Available online at www.sciencedirect.com
ScienceDirect
Colloids and Surfaces A: Physicochem. Eng. Aspects 294 (2007) 267–279
COLLOIDS AND SURFACES A
www.elsevier.com/locate/colsurfa

Effect of electrostatic interaction on deposition of colloid on partially covered surfaces Part II. Results of computer simulations

Paweł Weroński [a,b,*]

[a] Institute of Catalysis and Surface Chemistry, Polish Academy of Sciences, ul. Niezapominajek 8, 30-239 Kraków, Poland
[b] Center for Nonlinear Studies and Theoretical Division, Los Alamos National Laboratory, MS-B284, Los Alamos, NM 87545, USA

Received 26 July 2006; accepted 8 August 2006
Available online 15 August 2006

Abstract

We study random sequential adsorption (RSA) of electrostatically interacting colloid particles using the new simulation approach described in Paper I [P. Weroński, Effect of electrostatic interaction on deposition of colloid on partially covered surfaces. Part I. Model formulation, Coll. Surf. A 294 (2007) 254]. Numerical simulations are performed according to this curvilinear trajectory RSA model to determine the available surface function, jamming coverage, and pair-correlation function of the larger particles. The effect of the particle size ratio, electrolyte ionic strength, and the small-particle surface coverage on the large-particle deposition is demonstrated. The numerical results are tested using the two-dimensional (2D) scaled-particle theory, with a modification for the sphere geometry and electrostatic interaction, exploiting the extension of the effective hard-particle approximation to bimodal systems. The effect of electrolyte concentration on the effective minimum particle surface-to-surface distance is presented, too. The numerical results are compared with the results obtained using two older approaches, the 2D and three-dimensional (3D) RSA models. The study suggests that the formula stemming from the scaled-particle theory provides a good approximation in the low surface coverage limit. The results obtained with the 3D and curvilinear trajectory models indicate that large-particle/substrate attractive interaction significantly reduces the kinetic barrier to large, charged-particle adsorption at a surface precovered with small, like-charged particles. The available surface function and jamming-coverage values predicted using the simplified 3D and the more sophisticated curvilinear trajectory models are similar, while the results obtained with the 2D model differ significantly. The pair-correlation function suggests different structures of monolayers obtained with the three models. Results of this research clearly suggest that the extended curvilinear trajectory RSA approach can fruitfully be exploited for numerical simulations of colloid-particle adsorption at precovered surfaces, allowing the investigation of soft-particle systems.
© 2006 Elsevier B.V. All rights reserved.

Keywords: Adsorption of colloid particles; Particle electrostatic interaction; Colloid deposition; Monte Carlo simulation; Random sequential adsorption; RSA model

1. Introduction

In the preceding companion paper [1], hereafter referred to as Paper I, we discussed shortcomings of the existing two-dimensional (2D) and three-dimensional (3D) RSA models that can lead to inaccurate computational results, especially in the case of adsorption at a surface precovered with small, like-charged particles. We also introduced the new curvilinear trajectory (CT) RSA model that overcomes the shortcomings. In this paper we present results of the numerical simulations conducted using the CT RSA model. First, we describe the simulation algorithm in more detail. Our determinations of the effective minimum particle surface-to-surface distance, available surface function, jamming coverage, and radial distribution function are presented next. Lastly, we verify the effect of the particle size ratio, small-particle surface coverage, and electrolyte ionic strength on the characteristics of the adsorption process. The numerical results are tested in terms of the 2D scaled-particle theory, with a modification for the sphere geometry and electrostatic interaction, using equations derived in Paper I. The numerical results are compared with the results obtained using two older approaches, the 2D and 3D RSA models. This comparison allows us to evaluate the limits of applicability of the older models.

* Tel.: +1 505 667 9956; fax: +1 505 665 2659.
E-mail address: pawel@lanl.gov.

0927-7757/$ – see front matter © 2006 Elsevier B.V. All rights reserved.
doi:10.1016/j.colsurfa.2006.08.020

2. The simulation algorithm

The simulations of the irreversible adsorption process were carried out over a square simulation plane with the usual periodic boundary conditions at its perimeter and two subsidiary grids of square areas (cells) of the size $\sqrt{2}a_s$ and $\sqrt{2}a_l$ [2]. This strategy enhanced the scanning efficiency of the adsorbing particle environment performed at each simulation step. The simulations were conducted in two main stages: first, adsorption of smaller particles at the homogeneous interface was carried out to a desired surface coverage; then, the larger particles were adsorbed at the prepared heterogeneous surface. At both stages the surface coverage was calculated using the equation:

$$\theta_i = \frac{\pi a_i^2 N_i}{S}, \quad i = s, l, \tag{1}$$

where N_i is the number of spherical particles of radius a_i adsorbed at the interface of the area S. The subscripts s and l refer to small and large particles, respectively.

At both stages, the next particle to be adsorbed was selected by choosing at random its X_v and Y_v center coordinates. Next, the vicinity of the test particle was scanned, and the minimum distance $H_{min} = Z_{min} - 1$ to the interface, resulting from the non-overlapping condition, was calculated. Then the particle–interface interaction at the minimum distance was calculated as described in Paper I, using the limiting form of the equation:

$$E_{ij}(H_1) = \varepsilon \frac{kT}{e^2} Y_i Y_j \frac{a_j}{1 + a_j/a_i + H_1} \exp(-\kappa a_i H_1), \quad i, j = l, s \tag{2}$$

when one of the particles' radii tends to infinity and $H_1 = H_{min}$. In this equation ε is the dielectric constant of the medium, k the Boltzmann constant, T the temperature, e the electron charge, $\kappa^{-1} = \sqrt{10^3\, \varepsilon kT/(8\pi e^2 I N_A)}$ the Debye length in cm, I the electrolyte ionic strength expressed in mol/dm^3, N_A Avogadro's number, and Y_i and Y_j are the effective surface potentials of the interacting surfaces, respectively [1].

If the particle–interface potential at the minimum distance was larger than $E_{ip}(H_{min}) > -0.01$, i.e., the minimum distance H_{min} was large and the attraction to the interface was negligibly small compared with the particle–particle repulsion at the point (X_v, Y_v, $H_{min} + 1$), the virtual particle was rejected and new particle coordinates were generated. Otherwise, the location and height of the kinetic barrier to adsorption E_b was calculated for the virtual-particle energy profile represented by the equation:

$$E_i(H) = \sum_{m=1}^{n} E_{ij}(H_m) + E_{ip}(H), \quad i, j = l, s \tag{3}$$

at fixed X_v and Y_v coordinates, where $H = h/a_i$ is the particle–interface gap width expressed in particle radii a_i, n the number of the small and large particles attached to the collector surface in the vicinity of the adsorbing particle, H_m the minimum surface-to-surface distance between the moving particle and the deposited particle m, and E_{ij} is the electrostatic (repulsive) interaction energy between them, calculated according to Eq. (2). In this paper we will always use $i = l$ in case of $i \neq j$.

If the barrier existed, the starting point of the particle trajectory was assumed to be at the barrier. Otherwise, the particle–interface interaction was verified at the point (X_v, Y_v, $H_{min} + 1$). When the interaction was attractive, the particle was adsorbed at the point (X_v, Y_v, 1) and the next virtual coordinates were chosen; otherwise, the starting point was assumed to be at the minimum distance H_{min}, and the total particle potential was calculated at the point (X_v, Y_v, $H_{min} + 1$). Based on the value of the potential or barrier height, the probability of appearing of the particle at the starting point of the trajectory was calculated from the Boltzmann relationship. If the probability was smaller than an additional random number generated with uniform distribution within the interval (0; 1), the adsorption attempt was rejected, and the next virtual coordinates were chosen. Otherwise, the X_v and Y_v coordinate constraints were released and the particle trajectory was calculated to the particle's point of contact with the adsorption surface at $H = 0$, using the deterministic equation of motion:

$$\frac{d\mathbf{R_i}}{d\tau_i^*} = \mathbf{F_i}(\mathbf{R_i}), \tag{4}$$

where $\mathbf{R_i} = \mathbf{r_i}/a_i$ is the virtual-particle position vector in the a_i units, $\tau_i^* = t a_i^2 / D_i^\infty$ the dimensionless time, t the time in s, $D_i^\infty = kT/6\pi\eta a_i$ the diffusion coefficient of the particle in the bulk, η the solution dynamic viscosity, and $\mathbf{F_i}$ the net force acting on the particle, expressed in the kT/a_i units and calculated according to the equation:

$$\mathbf{F_i}(\mathbf{R_i}) = -\nabla E_i(\mathbf{R_i}), \tag{5}$$

where $E_i(\mathbf{R_i})$ is the total particle potential given by Eq. (3). Once the particle touched the interface, its position was permanently fixed, with no consecutive motion allowed.

In rare cases (one per a few thousands of trials) the particle was driven far from the adsorption surface. If the particle–interface interaction dropped to 10^{-2} kT, a new adsorption attempt was undertaken. Each particle path was calculated using the CT RSA model and taking into account only neighboring particles. The tested vicinity of the virtual particle was limited to a circle that included all the adsorbed particles for which E_{ij} could potentially be larger than 0.01.

This algorithm enabled us to simulate adsorption kinetics in terms of the dimensionless adsorption time defined by the expression:

$$\tau_i = \frac{\pi a_i^2}{S} N_{att}^i, \quad i = s, l, \tag{6}$$

where N_{att}^i is the overall number of the particle adsorption trials performed during the first or second adsorption stage. One should note that such computed kinetics neglects the coupling between the bulk and surface-layer transport and therefore can be directly used only in specific systems where the coupling is negligible. The maximum dimensionless time τ_l attained in our simulations was 10^4, which required an overall number of trials on the order of 10^9 to 10^{10}. The maximum surface coverage

reported later on corresponds just to the coverage achieved after $\tau_l = 10^4$.

Available surface functions were calculated using this algorithm and the method of Schaaf and Talbot [3] by exploiting the definition:

$$B_i(\theta_s, \theta_l) = \frac{N^0_{succ}}{N^0_{att}}, \quad i = s, l, \tag{7}$$

where N^0_{att} and N^0_{succ} are the overall and successful number of adsorption attempts, respectively, performed at fixed θ_s and θ_l. In our simulations these numbers were on the order of 10^5.

The data obtained with this algorithm allowed us to calculate the pair-correlation function (called also radial distribution function) defined in Ref. [4] as:

$$g_i(R_i) = \frac{S}{N_i}\left\langle \frac{\Delta N_i}{2\pi R_i \Delta R_i} \right\rangle, \quad i = s, l, \tag{8}$$

where angle brackets mean the ensemble average, ΔN_i is the number of particle centers within the ring $2\pi R_i \Delta R_i$ drawn around a central particle, and $R_i = r/a_i$ the dimensionless radius of the ring.

3. Results of computations

The CT RSA algorithm was used to perform extensive computer simulations of soft-particle adsorption at precovered surfaces. The available surface functions, jamming limits, and pair-correlation functions were obtained for the following values of the system's physical parameters: the large- and small-particle density and surface potential $\rho_l = \rho_s = 1.05\ \mathrm{g/cm^3}$ and $\psi_l = \psi_s = 50\ \mathrm{mV}$, respectively; the adsorption surface potential $\psi_p = -100\ \mathrm{mV}$; the absolute temperature $T = 293\ \mathrm{K}$; the dielectric constant $\varepsilon = 78.54$; and the large-particle radius $a_l = 500\ \mathrm{nm}$. The computations were conducted for three values of the small-particle radius: $a_s = 125$, 250, and 500 nm, corresponding to the particle size ratio $\lambda = 4$, 2, and 1. A few values of electrolyte concentration were chosen to demonstrate the effect of ionic strength. The values corresponded to the parameters $\kappa a_i = 4$, 8, 16, 32, 64, 125, 250, 500, 1000, and 2000. The effect of the small-particle surface coverage was verified for $\theta_s = 0$ (reference curves for monodisperse particle system), 0.02, 0.04, and 0.08.

The numerical results of the computations were compared with the analytical results stemming from the scaled-particle theory, extended to interacting spheres in 3D. Specifically, we used the formula for the available surface function in the low surface-coverage limit

$$B_l = (1 - \theta_d)\exp\left[-\frac{3\theta_{ld} + \gamma(\gamma+2)\theta_{sd}}{1-\theta_d} - \left(\frac{\theta_{ld} + \gamma\theta_{sd}}{1-\theta_d}\right)^2\right] \tag{9}$$

and its limiting form at $\theta_l = 0$

$$B^0_l = (1 - \theta_{sd})\exp\left[-\frac{\gamma(\gamma+2)\theta_{sd}}{1-\theta_{sd}} - \left(\frac{\gamma\theta_{sd}}{1-\theta_{sd}}\right)^2\right] \tag{10}$$

derived in Paper I. The variables θ_{ld}, θ_{sd}, and γ, appearing in these equations, are defined as:

$$\theta_{ld} = \left(\frac{d^*_{ll}}{2a_l}\right)^2 \theta_l, \quad \theta_{sd} = \left(\frac{d^*_{ss}}{2a_s}\right)^2 \theta_s, \quad \text{and} \quad \gamma = 2\frac{d^*_{ls}}{d^*_{ss}} - 1, \tag{11}$$

where the effective hard-particle center-to-center distance projection lengths d^*_{ij} were calculated by application of the Barker-Henderson or thermal-energy approximation to one of the RSA models [1]. The formula used for the 2D RSA model and the Barker-Henderson approximation was:

$$d^*_{ij} = a_i \int_0^\infty \{1 - \exp[-E_{ij}(R_2)]\}\mathrm{d}R_2, \quad i, j = s, l, \tag{12}$$

where $R_2 = \sqrt{(X_i - X_j)^2 + (Y_i - Y_j)^2} = \sqrt{R^2 - (1 - a_j/a_i)^2}$ is the dimensionless actual particle center-to-center distance projection length.

On the other hand, using the thermal-energy approximation we had

$$d^*_{ij} = a_i R^*_2, \quad E_{ij}(R^*_2) = 0.5. \tag{13}$$

In the case of the 3D RSA model and the Barker-Henderson approximation, we used the equation:

$$d^*_{ij} = a_i \int_0^\infty \{1 - \exp[-E_b(R_2)]\}\mathrm{d}R_2, \quad i, j = s, l. \tag{14}$$

In the high electrolyte-concentration limit, expressed usually in terms of the large κa_i parameter, the electrostatic interaction becomes weak, and the parameters d^*_{ij} tend to the nonzero values $2\sqrt{a_i a_j}$. Therefore, in this range of the κa_i parameter, a logarithmic plot of the functions $d^*_{ij}(\kappa a_i)$ becomes unreadable. To avoid this inconvenience, in what follows we present the effect of the κa_i parameter on the effective particle size in terms of the dimensionless effective minimum particle surface-to-surface distance,

$$H^*_{ij} = \frac{h^*_{ij}}{a_i} = \sqrt{\left(\frac{d^*_{ij}}{a_i}\right)^2 + \left(1 - \frac{a_j}{a_i}\right)^2} - 1 - \frac{a_j}{a_i}, \tag{15}$$

expected to be roughly proportional to the electric double-layer thickness.

The two older models, 2D and 3D RSA, were also exploited in the computations to allow comparison with CT RSA predicted results. It should be noted that at these particle sizes and density, the gravitational force acting on the particle was below 0.03 kT/a_i and therefore was neglected in our computations.

3.1. Effective minimum particle surface-to-surface distance

As discussed in Paper I, the effective minimum particle surface-to-surface distance is a very important parameter, characterizing the range of the particle–particle interaction. Qualitatively, the parameter can be defined as the average minimum distance at which particles can adsorb at the interface. Quantitatively, the parameter corresponds to the particle–particle distance at which the particle potential energy is on the order of the

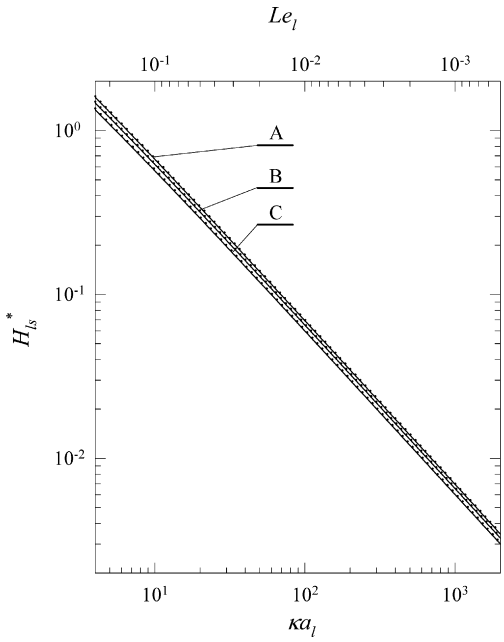

Fig. 1. Comparison of effective minimum distances between small and large particle at a plane interface, calculated according to the 2D model in connection with two effective hard-particle approximations. Solid lines depict the Barker-Henderson approach, Eqs. (15) and (12), and dotted ones represent the thermal energy approach, Eqs. (15) and (13). The effective distances H^*_{ls} correspond to $\lambda = 1$ (A), $\lambda = 2$ (B), and $\lambda = 4$ (C).

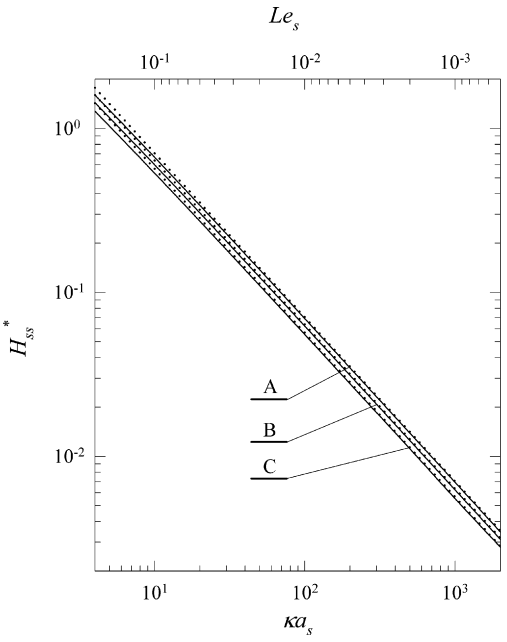

Fig. 2. Comparison of effective minimum distances between two small particles at a plane interface, calculated according to the 2D model in connection with two effective hard-particle approximations. Solid lines depict the Barker-Henderson approach, Eqs. (15) and (12), and dotted ones represent the linearized thermal energy approach, Eq. (16). The effective distances H^*_{ss} correspond to $a_s = 500$ nm (A), $a_s = 250$ nm (B), and $a_s = 125$ nm (C).

thermal energy. The potential energy, and therefore the effective minimum particle–particle distance, depends strongly on ionic strength of the electrolyte. The effect of ionic strength on the effective minimum particle surface-to-surface distance was studied by using the three models of adsorption and the two approximations of the effective hard particle. Fig. 1 presents the dependence of the normalized effective minimum distance $H^*_{ls} = h^*_{ls}/a_l$ on the κa_l parameter for three values of λ, as predicted by the 2D RSA model in connection with the two effective hard-particle approximations. The results based on Eq. (12) (the Barker-Henderson approach) and Eq. (13) (the thermal energy approach) clearly demonstrate that both approaches give almost identical results. As can be seen, the effect of λ is minor even at small values of κa_l, which suggests that the interface has little effect on particle adsorption, in line with the model's assumptions. The weak effect of the particle–interface interaction can also be deduced from the fact that the effective particle distances correspond well to the thermal energy $0.5\,kT$ in the whole range of the parameter κa_l. This value confirms the assumption of particle lateral equilibrium at the interface and results from neglecting the fast, curvilinear particle transport in the thin layer adjacent to the adsorption surface. In the presented range of the κa_l parameter, the dependence $H^*_{ls}(\kappa a_l)$ is almost linear. The results are limited to the range corresponding to $\kappa a_s \geq 4$ to avoid inaccuracies resulting from many-body interactions.

The linearity is more obvious in Fig. 2, where the normalized effective minimum distance $H^*_{ss} = h^*_{ss}/a_s$ as a function of the κa_s parameter is depicted, as obtained from the linearized thermal-energy approach, neglecting the preexponential term in Eq. (2). According to this approach, the effective minimum distance, corresponding to $0.5\,kT$ particle–particle energy, is given by the equation:

$$H^*_{ss} = \frac{1}{\kappa a_s} \ln\left(\frac{1}{2}\varepsilon\frac{kT}{e^2}Y_s^2 a_s\right). \tag{16}$$

As one can see, the effective minimum distance can be calculated analytically and is proportional to the parameter $Le_s = 1/\kappa a_s$. Comparison of the linearized approach and the nonlinear Barker-Henderson approximation shows that deviations of the function $H^*_{ss}(\kappa a_s)$ from linearity, as predicted from the 2D RSA model, are small and can be observed just at the small κa_s. The plots presented in Fig. 2 also demonstrate that the linearized thermal-energy approach offers a good approximation of the effective minimum particle surface-to-surface distance.

As discussed in Paper I, the perfect sink approximation exploited in the 2D RSA model seems to be valid only in the case of the large κa_i. Modeling adsorption in a system characterized by a larger interaction range, especially in a bimodal system, requires another approach. That is demonstrated in the next two figures, where the effect of ionic strength on the effective minimum interparticle distance is presented in the monodisperse and bimodal systems, using the 2D, 3D, and CT RSA models.

As can be seen in Fig. 3, in the case of monodisperse systems at high ionic strength ($\kappa a_s > 30$), both 2D and 3D models predict almost identical effective minimum distances, corresponding to the lateral interaction of about $0.5\,kT$. As discussed above, this value results from neglecting the nonlinear particle transport at the boundary layer. It should be kept in mind, however, that assuming the rectilinear particle trajectories in the 3D model could result in artificially lowering the effective interaction

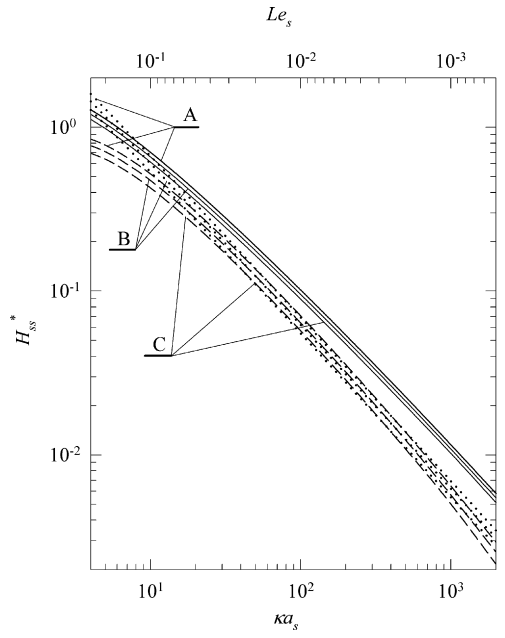

Fig. 3. Comparison of effective minimum distances between two small particles at a plane interface, calculated according to the Barker-Henderson approximation in connection with three RSA models. Dotted lines depict the 2D model, Eqs. (15) and (12); dashed lines denote the 3D model, Eqs. (15) and (14); and solid ones represent the CT model, Eqs. (15) and (4). The effective distances H^*_{ss} correspond to $a_s = 500$ nm (A), $a_s = 250$ nm (B), and $a_s = 125$ nm (C).

range. In fact, taking into consideration that at the energy barrier

$$\begin{cases} F_\perp = F_{lp} \\ E_{ls} + E_{lp} = E_b \end{cases} \tag{17}$$

(see Fig. 1a in Paper I) and exploiting the equations

$$F_{ls} = \frac{1+\kappa a_1 R}{R} E_{ls}, \quad F_{lp} = \kappa a_1 E_{lp},$$
$$F_\perp = \frac{1-1/\lambda+H}{R} F_{ls}, \quad F_{||} = \sqrt{F_{ls}^2 - F_\perp^2}, \tag{18}$$

where $R = 1 + 1/\lambda + H_{ls}$, one can find that the net force acting on the large particle at the energy barrier E_b is:

$$F_{||} = \kappa a_1 E_b \frac{\sqrt{R^2 - (1-1/\lambda+H)^2}}{R/[(\kappa a_1 R)^{-1}+1] + 1 - 1/\lambda + H}$$
$$\approx \kappa a_1 E_b \sqrt{\frac{2/\lambda + H_{ls} - H}{2 + H_{ls} + H}} \approx \kappa a_s E_b \sqrt{\lambda}. \tag{19}$$

The last formula was derived using inequalities $\kappa a_1 R \gg 1$, $2/\lambda \gg H_{ls} - H$, and $2 \gg H_{ls} + H$, which should be fulfilled in our systems at $\kappa a_s \geq 4$. Therefore, in monodisperse systems, the net force at the energy barrier is of the order $\kappa a_s E_b$ in the kT/a_s units and rapidly increases when the particle approaches the interface. Taking into account that the barrier height corresponding to the effective particle distance is about $E_b \approx 0.5$, one can deduce that at $\kappa a_s > 10$, the driving force is much larger than the kT/a_s unit, which is characteristic for thermal motion [5]. Therefore, Brownian motion can be neglected in considering fast-particle transport through the thin boundary layer at $\kappa a_s > 10$. Consequently, the equilibrium value of the interaction energy at the effective distance, as predicted by the 2D and 3D models, seems to have no solid support in theory.

On the other hand, in this range of κa_s the CT model predicts larger effective distances corresponding to the weaker particle–particle interaction. This prediction results from the fact that at the very beginning of the particle trajectory, the lateral, repulsive component of the net force $F_{||}$ dominates and moves the particle out of its quasi-equilibrium starting position. Simultaneously, the attractive component $F_\perp$, perpendicular to the interface, increases rapidly and moves the particle toward the surface. At condition $\kappa a_s > 10$, however, the boundary-layer thickness is much smaller than the particle radius; therefore, the adsorbing particle cannot approach the adsorbed one closely during the small displacement. As a result, the final particle positions correspond to interactions weaker than the thermal energy and to effective particle distances larger than predicted by the 2D and 3D models. It should be noted that at $\kappa a_s > 100$, the differences between the CT and 2D or 3D results become small in comparison with the particle size and can be hard to detect experimentally. Thus, one can claim that in the short interaction range, all the models offer a reasonable accuracy.

At $\kappa a_s < 10$ the net driving force at the energy barrier corresponding to the effective particle surface-to-surface distance becomes comparable to the kT/a_s unit, and Brownian motion may have some effect on particle adsorption. It should be noted, however, that just in this range of κa_s the effective distances correspond to the thermal energy, which suggests that the CT model offers a quite reasonable approximation even at the interaction range comparable to the particle size, in spite of neglecting Brownian motion. At this range of interactions, the effective particle distances predicted with the CT model become smaller than those predicted by the 2D model and correspond to the lateral repulsion a few times stronger than the thermal energy. This final position of the adsorbing particle results from the thicker surface-force boundary layer. At the thicker layer, the particle located at the effective energy barrier there is at a relatively large distance from the interface. Also, the particle center-to-center distance projection length R_2 is relatively small in such a position. After a short distance, when the adsorbing particle is mostly repulsed from its starting position, the attractive force starts to dominate and directs the particle almost perpendicularly to the interface. As a result, the adsorbing particle approaches the deposited particle closely, and the final position can correspond to a relatively high particle–particle potential.

As discussed above, the effective distance calculated with the 2D model corresponds to the lateral interaction on the order of thermal energy even at the smallest κa_s parameter, when the boundary-layer thickness becomes comparable to the particle dimension and one could expect the interface to have a strong effect. That value of the effective distance suggests overestimation of the results arising from the assumption of the constant parameter $\alpha = 0.5$, appearing in the formula that

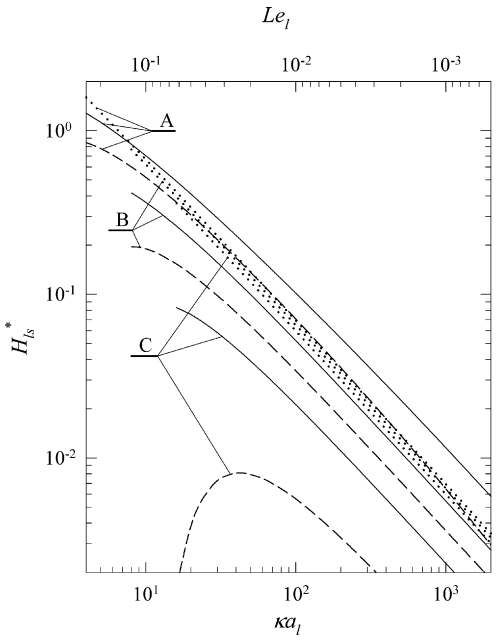

Fig. 4. Comparison of effective minimum distances between small and large particle at a plane interface, calculated according to the Barker-Henderson approximation in connection with three RSA models. Dotted lines depict the 2D model, Eqs. (15) and (12); dashed lines denote the 3D model, Eqs. (15) and (14); and solid ones represent the CT model, Eqs. (15) and (4). The effective distances H^*_{ls} correspond to $\lambda = 1$ (A), $\lambda = 2$ (B), and $\lambda = 4$ (C).

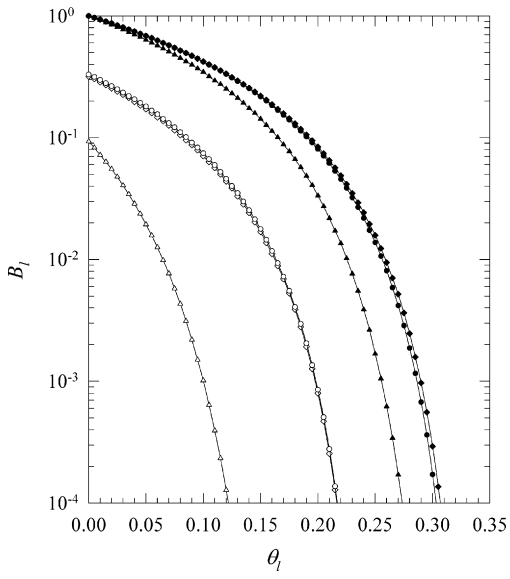

Fig. 5. Comparison of the available surface functions $B_l(\theta_l)$ computed with three RSA models for the particle size ratio $\lambda = 2$, parameter $\kappa a_l = 8$, and two values of the small particle surface coverage: $\theta_s = 0$ (filled symbols, reference curve) and $\theta_s = 0.08$ (open symbols). Triangles, diamonds, and circles correspond to 2D, 3D, and CT model predicted results, respectively, calculated with Eq. (7).

defines the electrostatic interaction in the 2D RSA model—see Eq. (3) in Paper I. The results obtained with the 3D model, on the other hand, corresponding to a lateral repulsion a few times stronger than kT, are evidently underestimated because of the assumption of the rectilinear particle trajectory.

The effect of the κa_l parameter on the effective minimum particle surface-to-surface distance H^*_{ls} in the bimodal systems is presented in Fig. 4. As discussed above, the 2D RSA model predicts the interface to have little effect on particle adsorption even at low ionic strength. On the other hand, the effect is evident in the cases of the 3D and CT models in the whole range of κa_l. In agreement with intuition, the large particle can be deposited next to the small one even at a lateral repulsion on the order of $10\,kT$, as predicted by the CT model. This behavior results from the strong attraction of the large particle to the interface, which partially compensates the repulsion exerted by the small particle. On the other hand, the effective distances calculated with the 3D model correspond to the lateral interaction, which is one to several orders of magnitude stronger than the thermal energy. Therefore, the rectilinear trajectory assumption in the 3D model does not seem reasonable, driving us to the conclusion that the CT RSA model offers the best description of colloid-particle adsorption. It should be noted that H^*_{ij} obtained from the CT RSA model refers to the final position of the adsorbing particle and thus conveys the information about the monolayer structure. On the other hand, H^*_{ij} calculated from the 3D RSA model corresponds to the available surface function, almost identical for both 3D and CT processes, and so allows kinetic characterization of the systems. This capability is discussed in more detail in the next section.

3.2. Available surface function

Comparison of the available surface functions derived from the 2D, 3D, and CT RSA models and computed for the parameters $\lambda = 2$ and $\kappa a_l = 8$ is presented in Fig. 5. The functions, calculated according to Eq. (8), refer to the parameter $\theta_s = 0$ (reference curve) and $\theta_s = 0.08$. In agreement with intuition, both 3D and CT models give identical results at $\theta_s = 0$ and low surface coverage of the large particle, which results from the similar construction of the algorithms. A small difference suggesting different monolayer structures becomes visible at $\theta_l = 0.15$. The difference grows with an increase of the surface coverage, so one could expect somewhat different jamming limits. As one can see, the available surface functions are always larger than their 2D counterparts, although the differences are very small at low surface coverage. This difference results from the fact that, unlike the 2D model, the 3D and CT models estimate the adsorption probability by taking into account the value of the particle potential calculated at some distance from the interface and therefore at larger particle–particle distance. Moreover, the interparticle repulsion is partially neutralized because of the attraction to the interface. The 2D model neglects the 3D effects. Therefore, it seems that application of the 2D model is limited to the monodisperse systems and low-to-medium surface coverage or high ionic strength ($\kappa a_s > 100$). On the contrary, the 3D model seems suitable for computing the kinetic aspects of adsorption in the full range of the κa_i parameters.

A similar behavior of the available surface functions may be observed at $\theta_s = 0.08$. Because of the different structures of the small particle layers, however, a small difference between the 3D and CT models is visible at the low surface coverage θ_l as well. Also, the difference between the predicted available surface functions for the 2D and 3D models is much larger in the bimodal

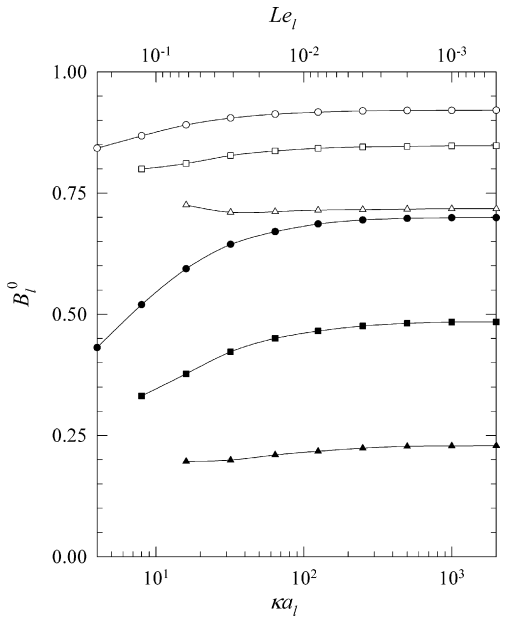

Fig. 6. Variation of the initial adsorption flux B_1^0 with the parameter κa_1 predicted by the model CT, Eq. (7). Open and filled symbols correspond to the small-particle surface coverage $\theta_s = 0.02$ and $\theta_s = 0.08$, respectively. The particle size ratio equals $\lambda = 1$ (circles), $\lambda = 2$ (squares), and $\lambda = 4$ (triangles).

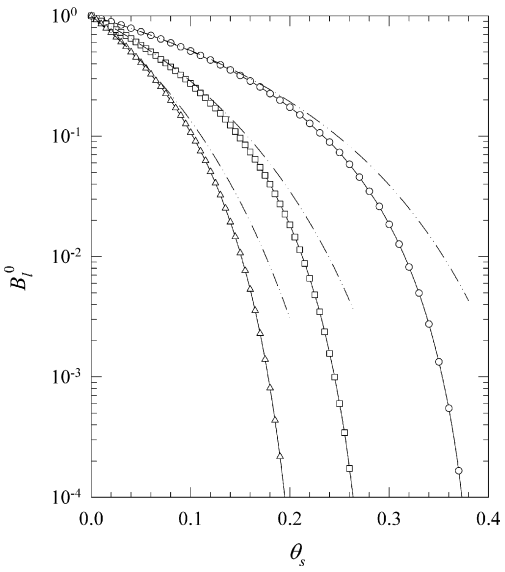

Fig. 7. Variation of the initial adsorption flux B_1^0 with the small-particle surface coverage θ_s for the particle size ratio $\lambda = 1$ (circles), $\lambda = 2$ (squares), and $\lambda = 4$ (triangles). Solid and dash-dot-dot lines denote results obtained in numerical simulations, Eq. (7), and using the scaled-particle theory equilibrium approach, Eq. (10), respectively.

system and reaches three orders of magnitude. This discrepancy suggests that unlike the 3D model, the 2D one is useless in the case of bimodal systems. This conclusion is consistent with the experimental results published in Ref. [6]. Although the authors of Ref. [6] suggested that the reduced blocking effect observed during deposition on the precovered surface could result from the small-colloid-particle charge migration at the mica surface, in view of the results presented here we can explain the observed effect as being based on the reduction of the different-size particles' repulsion at the charged adsorption surface.

The result, which can be considered as an aspect of the reverse salt effect [7], consisted in the enhancement of the particle deposition rate under attractive double-layer forces and experimentally proved at the end of the 1980s, is more evident in Fig. 6. The figure presents the initial deposition flux B_1^0 as a function of the κa_1 parameter, calculated according to the CT model for $\theta_s = 0.02$ and 0.08, at $\lambda = 1$, 2, and 4. At the hard-particle limit ($\kappa a_1 = 2000$), the results are in agreement with the limiting form of the available surface function at low surface coverage [1], i.e.,

$$B_1 \cong 1 - 4\lambda\theta_s, \tag{20}$$

apart from the two lowest curves corresponding to $\lambda = 2$ and 4 at $\theta_s = 0.08$, when $4\lambda\theta_s > 0.5$ and the assumption of low surface coverage does not apply anymore. In the long-interaction-range limit, on the other hand, the available surface function behavior depends on the λ parameter and is consistent with the dependences $H_{1s}^*(\kappa a_1)$, discussed above. At $\lambda = 1$, when H_{1s}^* is on the order of one, the available surface functions monotonically and relatively quickly decrease with κa_1, which means that the particle–interface attraction has a minor effect on the surface blocking. At $\lambda = 2$, when H_{1s}^* reaches few tenths, the large particle can be adsorbed at a much shorter distance from the small sphere, and so the blocking effect is reduced by the stronger particle-surface attraction. Indeed, the corresponding available surface functions' slopes are smaller than those when $\lambda = 1$, which confirms the statement. Finally, at $\lambda = 4$ one can observe that B_1^0 changes very little with κa_1, which means that the interparticle repulsion is neutralized by the attraction to the interface. As a matter of fact, the corresponding H_{1s}^* is below 0.09, which confirms the weak blocking effect. Moreover, the value of B_1^0 computed at $\lambda = 4$, $\theta_s = 0.02$, and $\kappa a_1 = 16$, is larger than the corresponding hard-particle limit. This fact means that, because of attraction to the interface, the particle can be adsorbed even if at the starting position it is located partially behind the small particle at $R_2 < 2/\sqrt{\lambda}$, which would be impossible in a hard-particle system. One should also note that the effect of attraction to the interface is smaller at the higher coverage θ_s, what results from the enhanced repulsion exerted by the larger number of the smaller particles.

The effect of the small-particle surface coverage and particle size ratio on the B_1^0 available surface function is investigated in Fig. 7. Both CT-model and equilibrium results – Eq. (10) – are presented there for $\kappa a_1 = 16$ and $\lambda = 1$ (reference system), 2, and 4. The results computed using the two models are essentially identical in the low surface-coverage limit, which confirms the robustness of the software used for simulations. At higher coverage, however, the equilibrium available surface functions achieve larger values, and the differences increase with the coverage θ_s. The available surface functions rapidly decrease with an increase in the λ parameter, which suggests that the presence of smaller (invisible) particles at the interface can result in a strong reduction of the adsorption flux. This surface poisoning effect should be experimentally detectable by a measurement of the large-particle initial adsorption flux.

However, a quantitative determination of the surface coverage of these particles becomes possible only by considering the coupling between the surface-layer transport (described by the function B_1^0) and the bulk transport (governed by convective diffusion of particles). According to the surface-force boundary-layer approximation [8], the actual initial particle flux j_1^0 in this case is governed by the generalized blocking function

$$\bar{B}_1^0(\theta_s) = \frac{j_1^0}{j_1^{0,0}} = \frac{KB_1^0(\theta_s)}{1+(K-1)B_1^0(\theta_s)}, \tag{21}$$

where $j_1^{0,0}$ is the initial adsorption flux to the homogeneous surface (at $\theta_s = 0$) and $K = k_a/k_b$, k_a is the kinetic adsorption constant given by the equation:

$$k_a = \left\{ a_1 \int_{H_{PM}}^{H_L} \frac{\exp[\phi_{lp}(H')]}{D_1(H')} dH' \right\}^{-1}, \tag{22}$$

where H_L and H_{PM} are the dimensionless thickness of the adsorbed small-particle layer and the primary minimum distance, respectively; ϕ_{lp} is the particle–interface potential; D_l the position-dependent diffusion coefficient of the large particle; $H' = H + H_{PM}$; and k_b the bulk mass-transfer rate. This rate can be calculated analytically or numerically for the stationary transport to uniformly accessible surfaces such as a rotating disk, impinging jet cells, etc. [9,10].

Expressing the diffusion coefficient as $D_l(H') = D_l^\infty H'/(H'+1)$ [11] and assuming the CT model of the electrostatic interaction, we can substitute $\phi_{lp} = E_{lp}$ and $H_L \approx 2/\lambda + H_{ls}^{0*}$, where $H_{ls}^{0*} = h_{ls}^{0*}/a_l$ is the effective dimensionless minimum particle surface-to-surface distance calculated for the isolated system of the small and large particles, located far from the interface. Then k_a can be evaluated explicitly to give:

$$K = \left[Sh \left(\ln \frac{2/\lambda + H_{ls}^{0*}}{H_{lp}^*} + \frac{2}{\lambda} + H_{ls}^{0*} - H_{lp}^* \right) \right]^{-1}, \tag{23}$$

where $Sh = k_b a_l / D_l^\infty$ is the dimensionless mass-transfer Sherwood number, and $H_{lp}^* = h_{lp}^*/a_l$ is the dimensionless particle–interface gap width corresponding to $E_{lp}(h_{lp}^*) = -0.5$. On the other hand, the perfect sink approximation exploited in the 2D model gives:

$$K = \left[Sh \left(\ln \frac{H_L}{H_{PM}} + \frac{2}{\lambda} \right) \right]^{-1}. \tag{24}$$

As can be deduced from Eq. (21), the large particle flux (normalized to the flux for an uncovered surface) depends on two unknown parameters only,

$$\frac{j_1^0}{j_1^{0,0}} = f(\lambda, \theta_s), \tag{25}$$

which suggests that by experimental measurements of $j_1^0/j_1^{0,0}$ for various large-particle sizes, we can determine both coverage θ_s and radius a_s of the small particle using a nonlinear fitting procedure.

Experimental data presented in Fig. 8, obtained for latex particles [12], confirm the validity of the above model, as well as the CT approach, for predicting the adsorption flux of larger particles at precovered surfaces. The experiments were conducted using the circular impinging jet cell and particles of 0.68 and 1.48 micron in diameter at $I = 10^{-4}$ M and the Reynolds number $Re = 4$. The dimensionless parameters were $\lambda = 2.2$ and $\kappa a_l = 24.55$. The surface potentials $\psi_s = \psi_l = -50$ mV and $\psi_p = 50$ mV were assumed in the computer simulation, according to the experimental conditions, which gave the effective distances $H_{ls}^{0*} = 0.305$ and $H_{lp}^* = 0.360$. The Sherwood number obtained by the numerical solution of the convective diffusion equation was $Sh = 0.0822$. Based on Eq. (23), we can calculate $K = 5.88$.

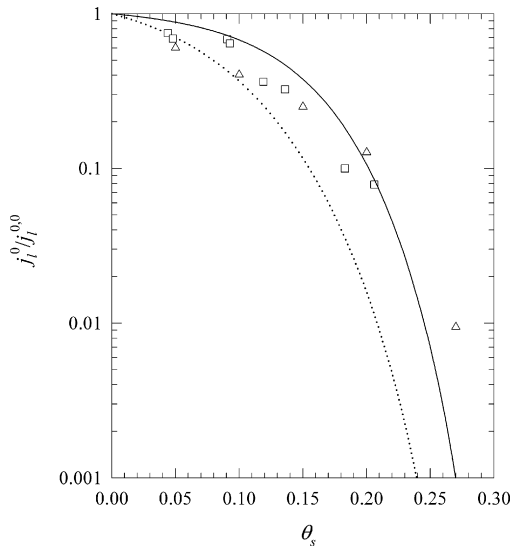

Fig. 8. Comparison of theoretical and experimental normalized initial adsorption fluxes as a function of the small-particle surface coverage θ_s. Open symbols (triangles and squares) depict two series of experiments. The solid and dotted lines denote results derived from the surface force boundary layer approximation, Eq. (21), exploiting the $B_1^0(\theta_s)$ functions calculated numerically with the CT and 2D model, respectively, Eq. (7). See more details in the text.

The theoretical curve plotted in Fig. 8 is a good approximation of the experimental results in the whole range of the coverage θ_s. The only large discrepancy (one order of magnitude) between the observed and calculated value of the initial flux appears at $\theta_s = 0.27$, which can be explained by considering small-particle size polydispersity. As estimated later on, the maximum coverage of the small particle is about 0.34, and so the θ_s should be considered high. At high surface concentration, however, particle size polydispersity plays a significant role. As demonstrated in Ref. [13], assuming the constant particle diameter at a size polydispersity of 10% results in a 10% overestimating of the actual maximum surface coverage. Therefore, one could expect that the actual θ_s is about 0.25; the experimental result then agrees well with theory.

On the contrary, the curve predicted by the 2D model and calculated for $K = 2.5$, according to Refs. [8,14], underestimates the experimental results at $\theta_s > 0.2$ by one order of magnitude and more, which results from overestimating the blocking effect, as discussed above. A reasonably good agreement of the 2D model and the experimental results at the low surface coverage may be a consequence of the fact that in this regime, the overall transport

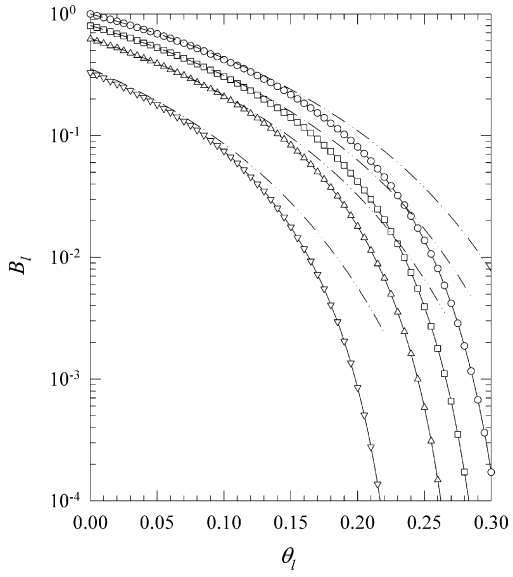

Fig. 9. Comparison of the available surface function $B_l(\theta_l)$ calculated using the CT model – solid lines, Eq. (7) – and the equilibrium scaled-particle theory – dash-dot-dot lines, Eq. (9) – for the particle size ratio $\lambda = 2$ and the parameter $\kappa a_l = 8$. Open symbols denote different values of the small-particle surface coverage: $\theta_s = 0$ (reference curve, circles), $\theta_s = 0.02$ (squares), $\theta_s = 0.04$ (triangles up), $\theta_s = 0.08$ (triangles down).

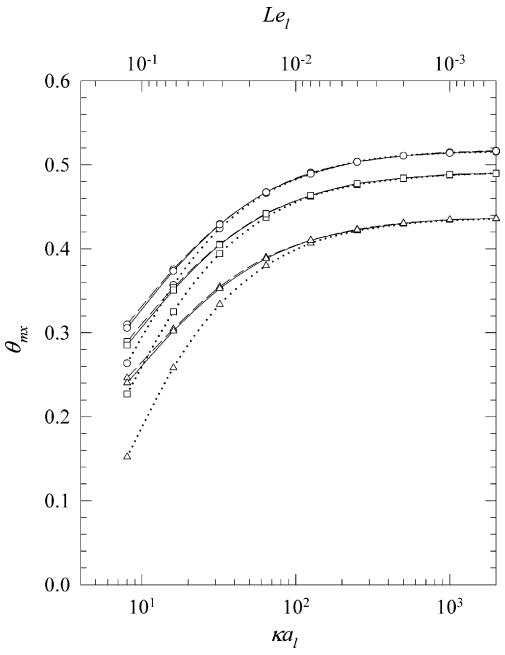

Fig. 10. Effect of the κa_l parameter on the maximum surface coverage θ_{mx} predicted by three RSA models: 2D (dotted lines), 3D (dashed lines), and CT (solid lines) at the particle size ratio $\lambda = 2$. Circles, squares and triangles correspond to the small-particle surface coverage $\theta_s = 0.02$, $\theta_s = 0.04$, and $\theta_s = 0.08$, respectively.

rate is determined mostly by convective diffusion because of a relatively small exclusion effect; thus, the inaccuracy introduced by the function B_l^0 is minor.

Fig. 9 presents the available surface functions $B_l(\theta_l)$ computed for our model systems. The functions were calculated using the CT RSA model and the equilibrium Eq. (9) for the bimodal systems characterized by the parameters $\lambda = 2$ and $\kappa a_l = 8$ at four different values of the coverage: $\theta_s = 0$ (reference curve), 0.02, 0.04, and 0.08. Based on the plots, conclusions similar to those found in Fig. 7 can be drawn. As one can see, both approaches give the same results within the limits of low surface coverage θ_s and θ_l. In the case of $\theta_s = 0.08$, however, the difference between both curves is evident even at $\theta_l = 0$. This difference results from the fact that the effective coverage corresponding to the system of the small particles is about 0.15, as can be estimated based on results obtained with the 3D model and presented in Fig. 3. In a similar way, one can estimate the effective size and coverage corresponding to the other curves. Therefore, we conclude that electrostatic interaction can significantly increase blocking effects in bimodal systems, especially at small λ and high surface coverage.

3.3. Maximum surface coverage

As with available surface functions, the maximum surface coverage that determines monolayer capacity is of great practical interest. As demonstrated in a number of earlier studies, the quantity depends very much on ionic strength. However, quantitative estimations of the dependence, published in scientific papers, are not consistent and change with the model of adsorption used in simulations or with the experimental procedure. The results stemming from the 2D, 3D, and CT models are compared in Fig. 10. They were obtained for the parameter $\lambda = 2$ at three values of the small-particle coverage: $\theta_s = 0.02$, 0.04, and 0.08. As mentioned earlier, the computations were conducted for a few values of the parameter κa_l and stopped after the dimensionless time $\tau_l = 10^4$. The reported values of θ_{mx} correspond to that time.

At high ionic strength, corresponding to the large parameter κa_l, all the models predict the same values of the maximum coverage, in agreement with intuition. This is the hard-particle limit. At the range of the low κa_l parameter, however, the results can be distinguished. Again, the plots obtained with the 3D and CT models are similar, whereas the 2D predicted results are much lower, which results from the overestimated blocking effects. Therefore, one can conclude that unlike the 2D model, the 3D model gives a reasonably good approximation of the maximum surface coverage at a lower computational cost, when compared with the CT model. The results are somewhat overestimated because of the assumption of the rectilinear particle trajectory, which can result in slightly higher coverage θ_{mx}. The maximum coverage θ_{mx} decreases with ionic strength and with an increase of the small-particle coverage θ_s.

The last conclusion can be drawn based on Fig. 11, as well. The results presented there were obtained using the CT model for two values of the coverage – $\theta_s = 0.02$ and 0.08 – and for three values of the parameter λ – 1, 2, and 4. As one may see, in the presented range of κa_l the effect of the parameter λ on the maximum surface coverage decreases with κa_l. The trend is consistent with the decrease of the effective particle size ratio λ^* at lower ionic strength, as described in Paper I. It is clear, however,

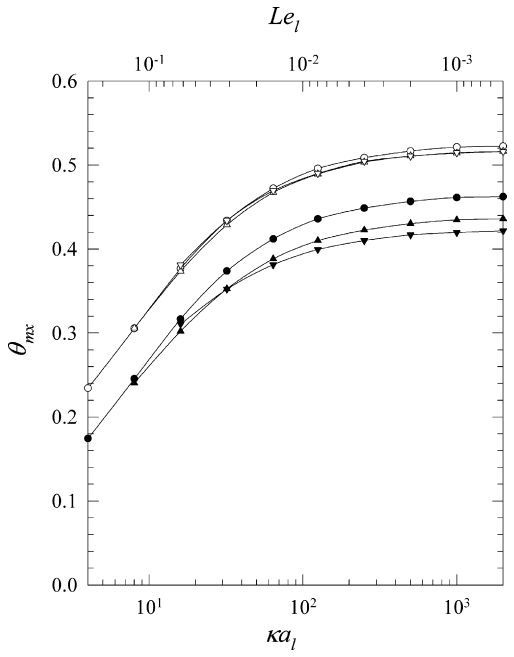

Fig. 11. Effect of the κa_l parameter on the maximum surface coverage θ_{mx} predicted by the CT model for three values of the particle size ratio: $\lambda = 1$ (circles), $\lambda = 2$ (triangles up), and $\lambda = 4$ (triangles down). Open and filled symbols denote results obtained at the small-particle surface coverage $\theta_s = 0.02$ and $\theta_s = 0.08$, respectively.

that the lowering of the effective size ratio does not explain why the plotted curves cross over one another. Obviously, at high ionic strength, when the particles can be considered hard, the maximum coverage decreases with increase of λ, as discussed in Ref. [15]. The opposite effect should be detectable at low ionic strength. It seems to result from the interplay between the particle–particle repulsion and the particle–interface attraction, as discussed above. At sufficiently low electrolyte concentrations, the smaller particles, corresponding to the larger λ, allow more-efficient interception of the large particle because of the rolling mechanism.

3.4. Pair-correlation function

Electrolyte ionic strength has a great impact not only on the kinetic aspects of large-particle adsorption but on controlling the formed monolayer structure, as well. As was demonstrated above, lowering the κa_i parameter results in a significant increase of the effective minimum particle surface-to-surface distance, which affects the pair-correlation function. In a real system, the function can be determined using experimental techniques. Therefore, by manipulating ionic strength one can easily verify a particle-deposition model in respect to both kinetics and structure. In actuality, the experimental determination of the correlation function is a difficult task because of the large number of particles needed to eliminate fluctuations and obtain a reasonably smooth curve. Moreover, some of the methods, like optical microscopy, have limited accuracy because of low image resolution, rarely exceeding a few tens of pixels per particle diameter. The effect of image resolution on $g_1(R)$ is

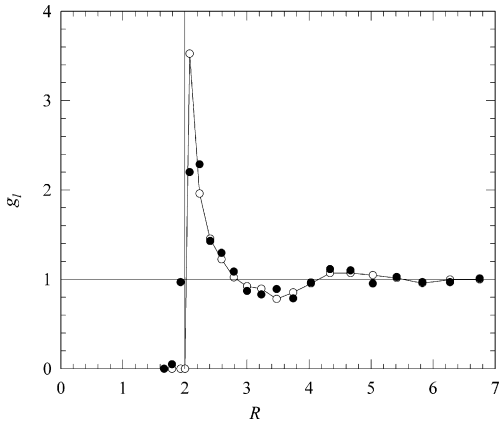

Fig. 12. Effect of picture resolution on the pair-correlation function. Open circles connected with a solid line represent the results obtained for the continuum particle coordinates (in the computer accuracy), and filled circles denote the values derived from the rounded-off particle coordinates (resolution of 10 pixels per particle diameter). Both functions are based on the same data obtained in the classical hard sphere RSA simulation. The number of particles used to compute the functions $g_1(R)$ is 2200, and the surface coverage $\theta_1 = 0.536$.

demonstrated in Fig. 12, where the pair-correlation function calculated for the hard particle monolayer close to jamming is compared with its counterpart obtained from the same simulation data at image resolution assumed to be 10 pixels per particle diameter. Note that rounding off the particle coordinates results in a significant change of the function profile, first of all in lowering of the primary maximum. The difficulties, however, are technical in nature and can be overcome with the further development of the experimental technique and electronics.

To begin with, Fig. 13 presents a comparison of the pair-correlation functions of the monodisperse system computed for the 2D, 3D, and CT models according to Eq. (8) for the following parameters: $a_1 = 500$ nm, $\kappa a_1 = 10$, and $\theta_1 = 0.25$. As one can see, the primary peaks are located at $R_p = r_p/a_1 = 2.9$, 2.7, and 2.85, as predicted by the 2D, 3D, and CT models, respectively. The positions correspond well to the effective

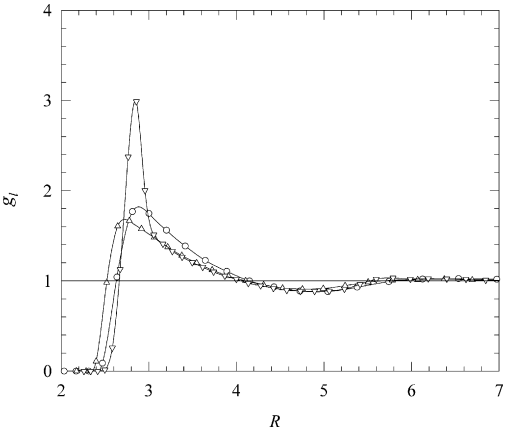

Fig. 13. Comparison of radial distribution functions $g_1(R)$ calculated using Eq. (8), based on simulation data obtained with three RSA models: 2D (circles), 3D (triangles up), and CT (triangles down). The results refer to the monodisperse system ($\theta_s = 0$) at the parameter $\kappa a_1 = 10$ and the large-particle surface coverage $\theta_1 = 0.25$.

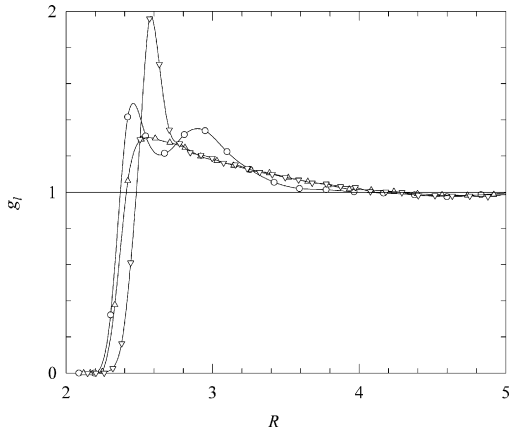

Fig. 14. Comparison of radial distribution functions $g_l(R)$ calculated using Eq. (8), based on simulation data obtained with three RSA models: 2D (circles), 3D (triangles up), and CT (triangles down). The results refer to the bimodal system at the particle size ratio $\lambda = 4$, small and large-particle surface coverage $\theta_s = 0.08$ and $\theta_l = 0.146$, and the parameter $\kappa a_l = 16$.

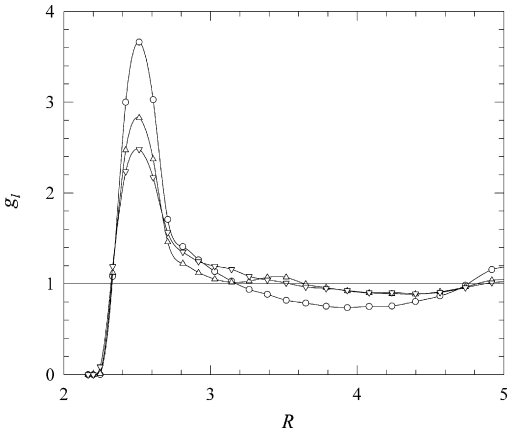

Fig. 15. Radial distribution functions $g_l(R)$ calculated using Eq. (8), based on data derived from CT simulations for the particle size ratio $\lambda = 1$ (circles), $\lambda = 2$ (triangles up), and $\lambda = 4$ (triangles down). The curves were computed at the small-particle surface coverage $\theta_s = 0.08$ and the parameter $\kappa a_l = 16$, close to jamming ($\tau_l = 10^4$).

minimum particle surface-to-surface distances, as presented in Fig. 11, and are equal to 2.65, 2.5, and 2.7, respectively. Assuming that the effective hard-particle radius equals half of the effective minimum distance, $a_l^* = 0.5h_{ll}^*$, all the peaks are located in the interval $r_p/a_l^* \in (2.1; 2.2)$, which agrees with the hard-particle result. The high maximum evident in the figure, obtained with the CT model, results from including the rolling effect in the model. In agreement with the algorithm and the available surface functions presented above, the correlation function computed with the 3D model is shifted toward the smaller interparticle distance, corresponding to the stronger lateral repulsion. At the particle–particle distance larger than three particle radii, both 3D and CT models give very similar results. All the three functions are basically indistinguishable at the distance larger than four radii, predicting the same position of the shallow minimum at $R = 4.8$.

The plots depicted in Fig. 14 were computed using the three models at the following parameters of the bimodal system: $\lambda = 4$, $\kappa a_l = 16$, $\theta_s = 0.08$, and $\theta_l = 0.146$. The primary maxima obtained for higher ionic strength are located at the smaller distances $R_p = 2.45$, 2.55, and 2.57 according to the 2D, 3D, and CT models, respectively. The corresponding effective minimum distances are equal to 2.42, 2.38, and 2.5 and comply with the peaks' position. The shift of the primary maximum toward the shorter interparticle distance, as well as the appearance of the secondary peak of the correlation function, demonstrates that the system computed with the 2D model is in the range of the high surface coverage achieved at a relatively long adsorption time. Again, this effect is a consequence of the stronger blocking effects in the model, resulting in the lower maximum coverage. One should note that the secondary maximum is located just one particle radius from the primary maximum, which suggests that its appearance is caused by the presence of the small particles. As in the monodisperse system, the CT model predicts a relatively high and sharp primary maximum, reflecting the particle-rolling effect. The 3D correlation function is shifted toward the smaller distance because it neglects that effect. The distance at which both functions can be considered identical is shorter than it was in the case of the monodisperse systems and corresponds to the shorter effective minimum particle surface-to-surface distance at higher ionic strength.

The pair-correlation functions appearing in Fig. 15 demonstrate the effect of particle size ratio as predicted by the model CT RSA at $\kappa a_l = 16$, $\theta_s = 0.08$, and $\theta_l = \theta_{mx}$. In agreement with intuition, the g_l function maximum position at $R = 2.5$ does not depend on λ and corresponds very well to the effective minimum particle distance. On the other hand, the peak height evidently decreases with an increase of the λ parameter. This can result from the fact that the tinier particles, more dispersed over the adsorption surface, cause larger irregularities in the large-particle structure. A very low secondary peak can be observed for $\lambda = 2$ at the distance $R = 3.5$, as can the heightened values of the correlation function corresponding to $\lambda = 4$ at the distance $R = 3$. As discussed above, the position of the deviations from the monodisperse functions suggests that their appearing is caused by the preadsorbed small particles. On the contrary, the correlation function obtained for $\lambda = 1$, with the secondary maximum located at a distance two times larger than the primary one, seems to be indistinguishable from its monodisperse counterpart.

The effect of ionic strength on correlation functions is presented in Fig. 16. The functions were computed for the parameters $\lambda = 4$, $\theta_s = 0.08$, and $\theta_l = \theta_{mx}$ at three values of the parameter κa_l: 16, 32, and 64, using the CT model. The primary maxima are located at $R = 2.5$, 2.3, and 2.15, respectively, and comply with the effective minimum distance depicted in Fig. 11. The peaks corresponding to the smaller parameter κa_l are lower and more diffused, in agreement with intuition. The heightened values of the correlation functions to the right of the peaks suggest an effect caused by the smaller, preadsorbed particles. Based on the figure, one may draw a more general conclusion that the presence of smaller particles at the adsorption surface can be manifested by an increase of the correlation function at the distance of about $R = R_{pp} + 2d_{ls}^*/a_l$, where R_{pp} is the primary

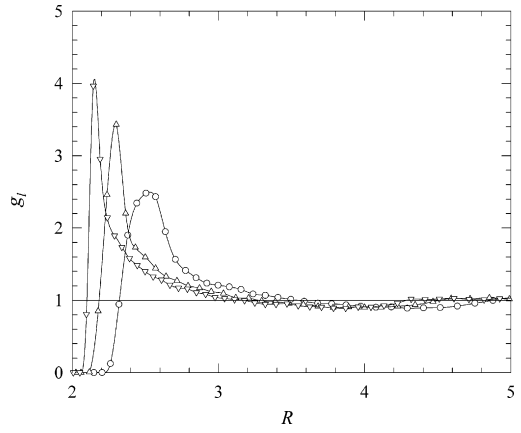

Fig. 16. Radial distribution functions $g_l(R)$ calculated using Eq. (8), based on data derived from CT simulations for the particle size ratio $\lambda = 4$ at three values of the parameter $\kappa a_l = 16$ (circles), $\kappa a_l = 32$ (triangles up), and $\kappa a_l = 64$ (triangles down). The curves were computed at the small-particle surface coverage $\theta_s = 0.08$, close to jamming ($\tau_l = 10^4$).

peak location. The effect becomes significant, however, at the higher coverage θ_l.

4. Conclusion

The analysis of the computational results obtained with the extended RSA models clearly suggests that these models are suitable for quantitative studies of adsorption on precovered surfaces in terms of the effective minimum particle surface-to-surface distance, available surface function, correlation function, and maximum coverage. In connection with the surface-force boundary-layer approximation, the models allow determination of the adsorption kinetics as well.

The simplest version of the model allowing the soft interaction is the 2D RSA model, which assumes the perfect sink particle-surface interaction and considers just the lateral particle–particle interaction. Consequently, this model overestimates the blocking effect and predicts the quasi-equilibrium pair-correlation function. Therefore, application of this model seems to be restricted to monodisperse systems and low surface coverage, as well as for systems where the particle/adsorption–surface interaction is very short ranged. The more sophisticated model, 3D RSA, which considers the electrostatic interaction particle–interface, adequately describes the kinetic aspects of adsorption in the full range of the κa_i parameter ($\kappa a_i > 4$). However, because the rectilinear particle trajectory is assumed, this model does not predict the correct correlation function, especially at high surface coverage. It seems that at present the best tool for studying the kinetic and structural aspects of adsorption is the CT RSA model, which includes the electrostatic particle–interface interaction and considers the curvilinear particle trajectory at a relatively low computational cost.

Results of computation suggest that the effect of electrostatic interaction on particle deposition at precovered surfaces depends substantially on ionic strength, the particle size ratio and surface coverage. At small-to-medium interaction range ($\kappa a_i > 10$) with a small λ parameter and medium-to-high surface coverage, when the interparticle repulsion dominates over the particle–interface attraction, electrostatic interaction effectively enhances the surface blocking effect. In the case of $\kappa a_i < 10$ and a large particle size asymmetry, however, the computations suggest domination of the attraction to the adsorption surface, which can result in a diminishing of the blocking effect, even in comparison with hard-particle systems. The effect is particularly noticeable at low surface coverage.

Application of the effective hard-particle concept allows extension of the scaled-particle theory for bimodal systems of soft particles. The derived analytical formulae for the available surface function are a good approximation of the numerical results in the range of low surface coverage.

The presence of small particles at the adsorption surface can be detected not only by measuring the adsorption flux or maximum coverage but also by determining the large-particle radial correlation function that becomes higher at the separation distance corresponding to two effective large particles with one small particle in between. In the case of the large coverage θ_l, a low secondary peak can even appear to the right of the primary maximum.

Acknowledgement

The author would like to thank Dr. B. Siwek for providing the experimental results, and Prof. J.Y. Walz for reading the manuscript and offering valuable suggestions. This work was partially supported by KBN Grant No. 3 T09A 089 27.

References

[1] P. Weroński, Effect of electrostatic interaction on deposition of colloid on partially covered surfaces. Part I. Model formulation, Coll. Surf. A 294 (2007) 254.
[2] P. Weroński, Kinetics of random sequential adsorption of interacting particles on partially covered surfaces, Bull. Pol. Ac. Chem. 51 (2003) 221.
[3] P. Schaaf, J. Talbot, Surface exclusion effects in adsorption processes, J. Chem. Phys. 91 (1989) 4401.
[4] Z. Adamczyk, P. Weroński, Random sequential adsorption on partially covered surfaces, J. Chem. Phys. 108 (1998) 9851.
[5] P. Schaaf, P. Wojtaszczyk, E.K. Mann, B. Senger, J.-C. Voegel, D. Bedeaux, Fluctuation of the number of adsorbed particles analyzed by a virial expansion: comparison between experiment and theory, J. Chem. Phys. 102 (1995) 5077.
[6] Z. Adamczyk, B. Siwek, P. Weroński, Adsorption of colloid particles at partially covered surfaces, J. Coll. Interf. Sci. 195 (1997) 261.
[7] Z. Adamczyk, B. Siwek, M. Zembala, P. Warszyński, Enhanced deposition of particles under attractive double-layer forces, J. Coll. Interf. Sci. 130 (1989) 578.
[8] Z. Adamczyk, P. Weroński, Application of the DLVO theory for particle deposition problems, Adv. Coll. Interf. Sci. 83 (1999) 137.
[9] Z. Adamczyk, B. Siwek, M. Zembala, P. Belouschek, Kinetics of localized adsorption of colloid particles, Adv. Coll. Interf. Sci. 48 (1994) 151.
[10] Z. Adamczyk, P. Warszyński, L. Szyk-Warszyńska, P. Weroński, Role of convection in particle deposition at solid surfaces, Coll. Surf. A 165 (2000) 157.
[11] B. Senger, P. Schaaf, J.-C. Voegel, A. Johner, A. Schmitt, J. Talbot, Influence of bulk diffusion on the adsorption of hard spheres on a flat surface, J. Chem. Phys. 97 (1992) 3813.

[12] Z. Adamczyk, B. Siwek, P. Weroński, M. Zembala, Adsorption of colloid particle mixtures at interfaces, Progr. Coll. Polym. Sci. 111 (1998) 41.
[13] Z. Adamczyk, B. Siwek, M. Zembala, P. Weroński, Influence of polydispersity on random sequential adsorption of spherical particles, J. Coll. Interf. Sci. 185 (1997) 236.
[14] Z. Adamczyk, Irreversible adsorption of particles, in: J. Toth (Ed.), Adsorption: Theory, Modeling and Analysis, Marcel-Dekker, New York, 2002, p. 251.
[15] Z. Adamczyk, P. Weroński, E. Musiał, Colloid particle adsorption on partially covered (random) surfaces, J. Coll. Interf. Sci. 241 (2001) 63.